ROYAL SOCIETY
OF CHEMISTRY

PAPER

Check for updates

Exploring the chemical and structural change of copper porphyrins upon charging by means of synchrotron X-ray absorption spectroscopy†

Thomas Smok, [ID] *[ab] Yang Hu, [ID] [a] Saibal Jana,[b] Frank Pammer[a] and Maximilian Fichtner [ID] *[ab]

In response to the growing demand for battery materials, researchers explore alternative resources with a focus on sustainability. Among these, organic electrode materials including porphyrins have emerged as promising candidates due to their advantageous properties, such as rapid charging capabilities and high energy densities. However, despite their potential, the precise charging mechanism of these alternatives remains elusive. To address this gap, our study delved into copper porphyrins, with a primary focus on [5,15-bis(ethynyl)-10,20-diphenylporphinato] copper(II) (CuDEPP). Employing synchrotron X-ray absorption spectroscopy in *operando* mode, we probed the evolution in chemical and electronic structure of Cu in CuDEPP. Our findings unequivocally demonstrate the participation of copper as a redox center during reversible charge storage, shedding light on its superior electrochemical performance. Furthermore, a combined approach involving extended X-ray absorption fine structure (EXAFS) studies and theoretical calculations provided deeper insights into the observed structural distortion during the charge storage process. Notably, our results support the hypothesis that redox processes, specifically those involving the aromatic porphyrin ring, drive the electrochemical activity of CuDEPP. In summary, our investigation offers important insights into the charging mechanism of copper porphyrins an essential step toward advancing sustainable organic materials for batteries.

1. Introduction

In recent times organic electrode materials (OEMs) have garnered significant attention due to their diverse properties, making them integral to various energy storage systems as they display many advantages.[1–4] They can be sustainably prepared from abundant, non-hazardous precursors found in nature[5,6] and their production processes can align with environmentally friendly practices, so the carbon footprint of this class of materials can be strongly reduced.[7–9] One key feature of OEMs lies in their adaptability. OEMs can be readily modified to suit specific applications, a crucial aspect in the ever-evolving landscape of energy storage.[10–12] Notably, OEMs serve as an alternative to conventional inorganic materials, particularly in the realm of multivalent batteries and post-lithium chemistries.

Their unique ability to accommodate larger, polarized ions with sluggish kinetics sets them apart.[13–15]

Porphyrins are representing an emerging type of OEMs which have due to their rapid storage behavior already demonstrated remarkable results as bridging materials between supercapacitors and batteries.[16–18] Their rapid charge storage hinges on the narrow energy gap between the highest occupied molecular orbital (HOMO) and lowest unoccupied molecular orbital (LUMO), what allows electrons easy transition between the two states.[16] As a representative of bipolar materials (b-type),[19] porphyrins combine high specific capacities typical for n-type materials with the high voltages characteristics of p-type materials.[20] This leads to high energy densities which are comparable to the ones obtained with inorganic materials.[20,21] The proposed charging mechanism of porphyrins centers around an aromaticity switch. Upon oxidation or reduction, the original neutral species, with its 18π electrons, transforms into a non-aromatic or antiaromatic form.[16,21] Interestingly, the electron transfer is not connected to a specific functional group, but appears delocalized over the whole conjugated ring of the porphyrin. 5,15-Bis(ethynyl)-10,20-diphenylporphinato copper(II) (shortly: CuDEPP) is one of the most well studied porphyrins in the field of electrochemical energy storage. CuDEPP has proven that it can be efficiently used

[a] *Helmholtz Institute Ulm (HIU), Electrochemical Energy Storage, Helmholtzstraße 11, 89081 Ulm, Germany. E-mail: m.fichtner@kit.edu, thomas.smok@kit.edu*

[b] *Institute of Nanotechnology, Karlsruhe Institute of Technology, Hermann-von-Helmholtz-Platz 1, 76344 Eggenstein-Leopoldshafen, Germany*

† Electronic supplementary information (ESI) available. See DOI: https://doi.org/10.1039/d4ya00242c

in monovalent Li,[21] Na,[17] K[22] ion batteries. In addition, it has been demonstrated that porphyrin materials can store multivalent ions as exemplified in rechargeable magnesium or calcium batteries.[23,24] Interestingly, it was often reported that copper porphyrins outperformed base-free porphyrins as well zinc porphyrins when it comes to capacity but also in regard to other important battery criteria like reversibility and cycling stability.[20,24–27]

To gain more insights, we investigated CuDEPP by means of *operando* X-ray absorption spectroscopy (XAS) at Cu K-edge to elucidate Cu-centered redox reactions and the local structure around the metal center. The beneficial role of the copper central atoms for the electrochemical performance of porphyrins as active material in batteries was recently reported,[28] and we provide evidence for the redox activity of copper. Furthermore, by meticulously analyzing the extended fine-structure region of the XAS spectra (EXAFS region), we gained valuable insights into the neighboring atoms of copper and interlinked the changes of the local structure of CuDEPP. Notably, our observations align with the previously proposed charge storage mechanism,[21] which refers to a reversible alteration of the aromaticity of the porphyrin ring. Therefore, our research sheds light on the charging mechanism of copper porphyrins, underscoring their high potential in advancing sustainable energy storage solutions.

2. Experimental

2.1. Materials

CuDEPP was synthesized after a method previously described in literature.[21] All other porphyrin materials presented in this study were received commercially from Porphychem SAS (France). Conductive carbons (Ketjenblack EC600JD, AkzoNobel; SuperP, Alfa Aesar, 99+ % on metal basis) were dried for at least 12 h in 300 °C in vacuum. The binder, in this case sodium-carboxymethyl cellulose (CMC, Sigma Aldrich; $M_w \approx 250$ kDa) was used without further purification.

2.2. Materials characterization

Powder X-ray diffraction (XRD) patterns were recorded in Debye–Scherer mode using a STOE STADI-P diffractometer (operated at 50 kV, 40 mA), equipped with a Mo Kα radiation source ($\lambda = 0.7093$ Å). For *ex situ* XRD measurements the cells were disassembled in an Ar-glovebox. The residual electrolyte salt on the cathodes was washed with anhydrous DME for three times and the dried powder was filled into capillaries and sealed. These steps were also performed under argon atmosphere.

2.3. Computational methodology

Density functional theory (DFT) computations were executed to explore molecular and periodic geometries. Molecular DFT analyses were conducted employing the Orca 5.0.1 software package,[29] employing the B3LYP-D3(BJ)/def2-TZVP level of theory.[30–34] This method integrates the hybrid functional B3LYP, the triple-ζ quality basis set def2-TZVP, and the third generation of Grimme's empirical dispersion correction (D3)

with the Becke–Johnson damping function (BJ). The attained structures were verified as local energetic minima through frequency calculations. Periodic DFT computations were performed within the generalized gradient approximation of the Perdew–Burke–Ernzerhof (GGA-PBE) method.[35] The Brillouin zone was sampled using a $4 \times 2 \times 2$ *k*-point grid according to the Monkhorst–Pack scheme,[36] as implemented in the Vienna *ab initio* simulation package (VASP 6.2.1).[37] The interaction between ion cores and valence electrons was modeled using the projector augmented wave (PAW) method[38] with a kinetic energy cut-off of 500 eV for all calculations. The energy convergence criterion for achieving fully relaxed geometry was set at 10^{-6} eV, while that for atomic forces was 10^{-2} eV Å^{-1}. Spin polarization was considered throughout the calculations, and van der Waals interactions were accounted for using the DFT-D3 approach.[32]

2.4. Electrode preparation

Two different types of electrodes were prepared for this study: In one method electrode discs with high loadings up to 20 mg cm^{-2} were casted. For this purpose, a slurry containing CuDEPP, SuperP and CMC in a weight ratio of 9:1:1 was mixed in water for 20 minutes at 200 rpm in a planetary centrifugal mixer (Thinky ARE-250). The slurry was blade casted on carbon coated aluminum and pre-dried under atmospheric conditions. Disks with a diameter of 11.8 mm (total loading up to 20 mg cm^{-2}) were cut and dried at 80 °C for 12 h in vacuum.

In the second method electrodes were pressed into pellets of 11 mm diameter. The raw materials CuDEPP, Ketjenblack and CMC (weight ratio 5:4:1) were mixed intensively in an agate mortar and pressed into pellet using a hydraulic press machine. The whole procedure was performed in an argon filled glovebox. The obtained pellets had a loading up to $\sim$10 mg cm^{-2}.

2.5. *In situ* cell

CR-2032 type coin cells (CR2032) with double Kapton windows of a diameter of 5 mm and a thickness of 30 μm were used for the *operando* XAS measurements. The cells were constructed with Li metal foil discs (14 mm diameter) as anodes and Celgard® 3501 separators. The electrolyte was 1 M LiPF$_6$ salt dissolved in ethylene carbonate (EC), propylene carbonate (PC) and dimethyl carbonate (DMC) in a volume ratio of 1:1:3 (V(EC):V(PC):V(DMC)). The coin-cell assembly was conducted in an argon-filled glovebox.

2.6. Synchrotron X-ray absorption spectroscopy

2.6.1. Beamline set up. X-ray absorption spectroscopy was carried out at the ROCK beamline of the French SOLEIL Synchrotron facility. The storage ring was operated in uniform Top-up mode at 2.75 GeV with a 500 mA current. ROCK is a beamline dedicated to *operando* XAS, thanks to the three quick-exafs monochromators in which the hard X-Ray photons come from a super bending magnet (2.81 T).[39,40] The beam is horizontally focused due to a collimating toroidal Ir coated mirror and the harmonics are removed by two mirrors tiled at 2.8 mrad using the B4C stripes. The beam size was 1.2 mm in

Table 1 Porphyrin and phthalocyanine reference standards

Materials	Label	Formula
5,15-Bis(ethynyl)-10,20-(diphenyl)porphyrin copper(II)	CuDEPP	$C_{36}H_{20}N_4Cu$
5,10,15,20-(Tetraphenyl)porphyrin copper(II)	CuTPP	$C_{44}H_{28}N_4Cu$
5-,10-,15-,20-(*meso*)-Tetra(4-ethynyl)porphyrin copper(II)	CuTEPP	$C_{28}H_{12}N_4Cu$
5-,10-,15-,20-(*meso*)-Tetra(4-carboxyphenyl)porphyrin copper(II)	CuTCPP	$C_{48}H_{28}N_4O_8Cu$
5,10,15,20-(Tetra-4-aminophenyl)porphyrin copper(II)	CuTAPP	$C_{44}H_{32}N_8Cu$
2,9,16,23-Tetra(amino)phthalocyanine copper(II)	CuTAPHT	$C_{32}H_{20}N_{12}Cu$

horizontal and 600 μm in vertical (both FWHM) at the sample position.

A Si(111) Quick-EXAFS monochromator was used with a oscillation speed of 2 Hz at the Cu K-edge enabling the collection of one full XAFS spectrum in 250 ms. As attenuator CVD 250 μm was applied in front of the Si monochromator. The signal was collected in transmission using three gas ionization chambers as detectors, which in series allowed the simultaneous recording of the incident beam, the beam transmitted by the sample, and the beam transmitted by a sheet of Cu metal foil; the latter was used as a reference for energy calibration.

2.6.2. XAS measurement. Transmission samples of reference standards, pristine materials and *ex situ* cycled electrode tapes (Table 1) were prepared by diluting powders with cellulose and pressing them into pellets. They were sealed in polyethylene bags inside an Ar-filled glovebox together with the pre-cycled electrode tapes. Samples were taken out of the glovebox shortly before being measured *ex situ*. The absorption spectra were averaged over more than 1000 scans (exposure $\sim$ 300 s).

2.6.3. *Operando* XAS. Cyclic voltammetry (CV) was performed on the *operando* cell using a Biologic VMP-3 potentiostat (Fig. 1). Cycling rates from 1 mV s^{-1} to 0.3 mV s^{-1} were applied over the voltage window 1.8–4.5 V. Cu K-edge XAS were measured continuously upon cycling and the extracted spectra were averaged over 200 scans (elapsed time 100 s, exposure 50 s). The extracted spectra have the energy grid as listed in Table 2.

2.6.4. Data analysis. XAS spectra were further analyzed using Fastosh,[41] Athena & Artemis packages[42] and Larch[43] software. Normalization was performed by regressing polynomials to the data before and after the edge step, then subtracting the pre-edge polynomial from the spectra and dividing by the edge jump. The calibrated and normalized near-edge X-ray absorption spectra (XANES) were compared with reference standards to fingerprint the chemical shifts and the electronic structure changes. Principle components analysis (PCA) and multivariate curve resolution by alternating least squares (MCR-ALS) were performed on normalized spectra from the *operando* measurements to extract the possible intermediate constituents and their evolution during cycling.

EXAFS spectra were extracted using the AUTOBK algorithm[44] and further Fourier transformed (FT) after applying a Hanning window function over an appropriate data range (Table 3). In order to probe the local structure and coordination environment for Cu, shell fitting was performed using theoretical models computed by FEFF8 in Larch.[43,45] More details are described in ESI.†

3. Results and discussions

3.1. Structure

Porphyrin materials are recognized for their distinctive crystallinity resulting from self-assembly into larger structures.[46,47] CuDEPP for example occurs in a triclinic crystal system within $P\bar{1}$ space group.[21] These materials can subsequently arrange into layered compounds as illustrated in Fig. 2a. This layered architecture is beneficial for hosting ions rendering it a principal driver behind their widespread application in energy storage.[48,49]
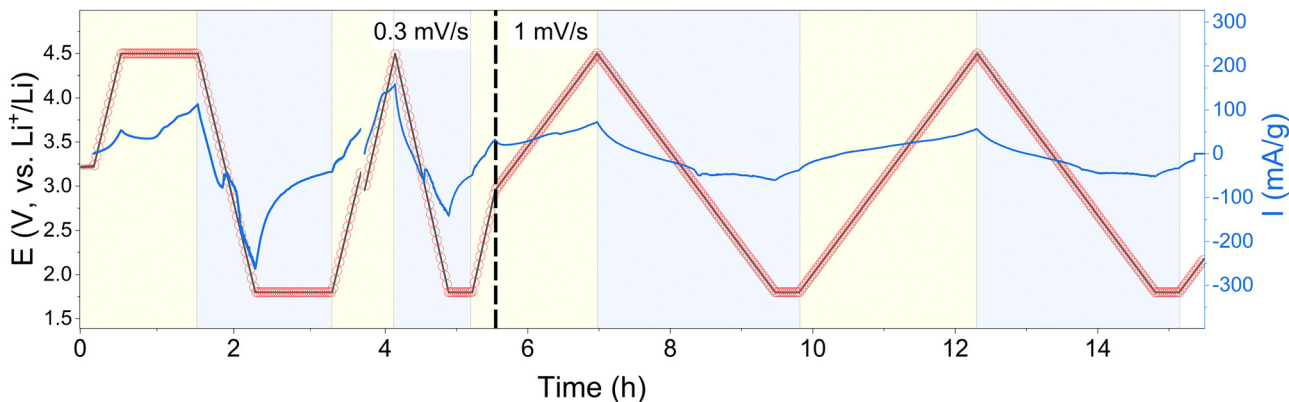

Fig. 1 Timeline of the cell voltage and response current during the *operando* XAFS measurement of the *in situ* cell (Cell number: TS-YH-012). Cu K-edge *operando* XAS on CuDEPP electrode during the cyclic voltammetric cycling: red and blue curve represent the voltage and current, respectively; read circle indicate the XAS acquisition; the scan rate was increased from 0.3 mV s^{-1} to 1 mV s^{-1} after the first cycle.

Table 2 Energy grid for the extracted Cu K-edge absorption spectra

Region	Operando		Ex situ	
	Range (eV)	Steps (eV)	Range (eV)	Steps (eV)
Pre-edge	8720–8970	2	8750–8970	2
Near-edge	8970–9016	0.2	8970–9016	0.1
Post-edge	9016–9640	2	9016–9930	1

Table 3 EXAFS extraction data

Samples	Data range		Fourier transform (FT)	
	E-range (eV)	k-space (Å^{-1})	Range (Å^{-1})	Window function
Ex situ	8950–9930	0–15	3–12	Hanning, 2
Operando	8920–9640	0–12	3–11.2	Hanning, 2

Further observing the intermolecular arrangement, calculations indicate the formation of larger structures like shown in the extended staircase model (Fig. 2b).[50]

Upon cycling these ordered structures get deteriorated and a reduction in crystallinity can be observed (Fig. S1, ESI†). Computational analyses reveal that porphyrin molecules undergo distortions of their molecular structure as bending upon ion storage within their framework (Fig. S2 and S3, ESI†). This effect is particularly pronounced during the insertion of PF_6^--anions with larger radii but can be also observed for lithium ion storage.
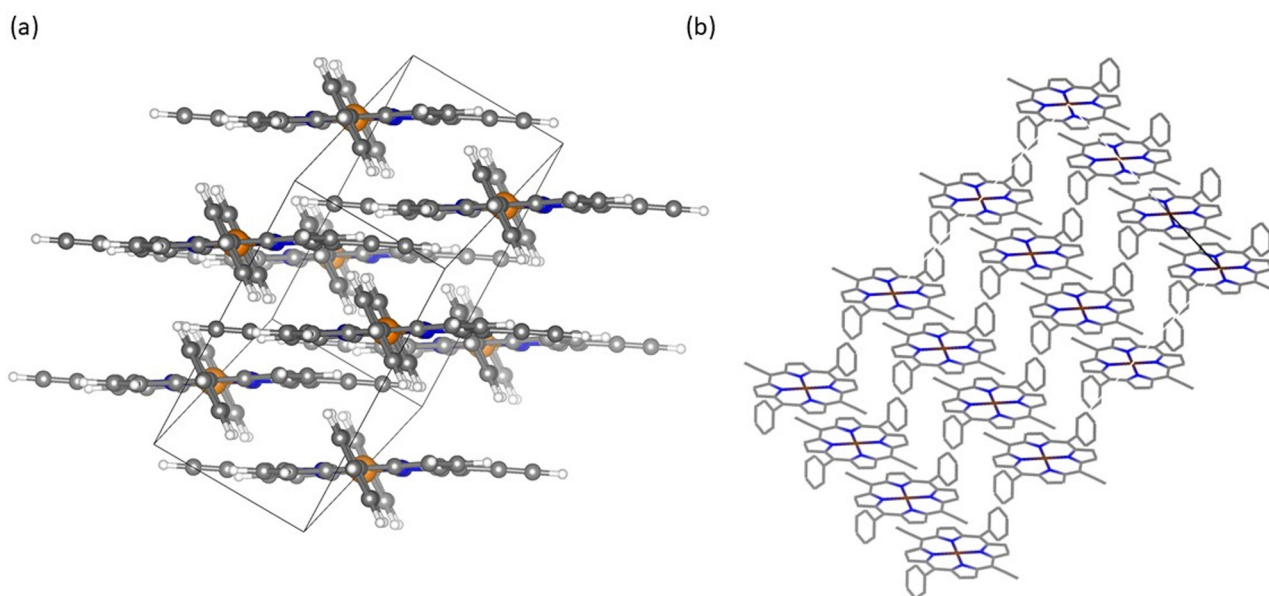
3.2. Cu K-edge XAS of porphyrin materials (Referencing)

The pristine porphyrin materials and as well as Cu(I) and Cu(II) standards were measured first as references (Fig. 3a). Most porphyrin materials including CuDEPP exhibited an edge energy close to Cu(II) standards (Fig. 3b), However, for 2,9,16,23-tetra(amino)phthalocyanine copper(II) (CuTAPHT) an exception

arose, which demonstrated a probably mixed Cu(I/II) state. Besides for CuTAPHT, the Fourier transformed k^2-weighted $\chi(k)$ spectra (Fig. 3c), demonstrated similar $|\chi(R)|$ owing to comparable local structure of Cu in pristine state. When focusing on the discharged materials, already during the analysis of ex situ CuDEPP samples, a change in the local structure could be observed. This observation suggested a local structure modification characterized by increased disorder upon lithiation. Comparing the $|\chi(R)|$ of pristine, carbon-mixed and charged (4.5 V) CuDEPP, similar values for amplitude and radial distribution were found, whereas a distinct difference from the discharged electrode was observed (Fig. 3d).

3.3. Operando XANES

To further investigate the change of the oxidation state of copper during cycling, CuDEPP was measured with synchrotron XAS in operando mode (Fig. 4). Within the XANES region near the copper edge, a discernible shift in the spectra toward lower energies emerged from the first cathodic scan onward. The isosbestic points in XANES spectra also suggested the reactions involved two governing species with varying concentration contributing to the total absorption.[51] Initially, CuDEPP harbored copper in the +II state. When further charged and therefore oxidized, as expected, no changes in the state of copper can be observed. During the discharge a transformation toward a mixed valence state in the electrode—comprising both +I and +II states—became evident. This observation aligns with the reference measurements presented earlier (in Fig. 4a and b). The most pronounced alterations manifested in the pre-edge and edge region, spanning energies between 8975 and 8995 eV. Interestingly, the reduction during discharge and subsequent oxidation during charging appear to be reversible across cycles. However, it is important to note two key points. Firstly, the initial state is not fully restored, implying that the material does not

(a)   (b)

Fig. 2 Layered CuDEPP-structure (a) and extended staircase model (b) obtained by DFT-calculations.
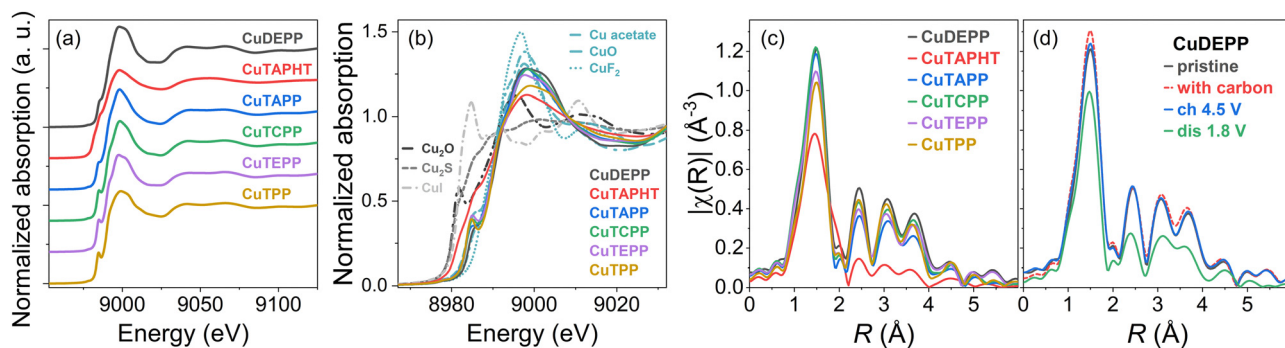
Fig. 3 *Ex situ* Cu K-edge absorption spectra of porphyrin materials (a) and reference standards (b). The Fourier transformation $|\chi(R)|$ spectra of the corresponding porphyrin materials (c) and cycled *ex situ* CuDEPP electrodes (d).
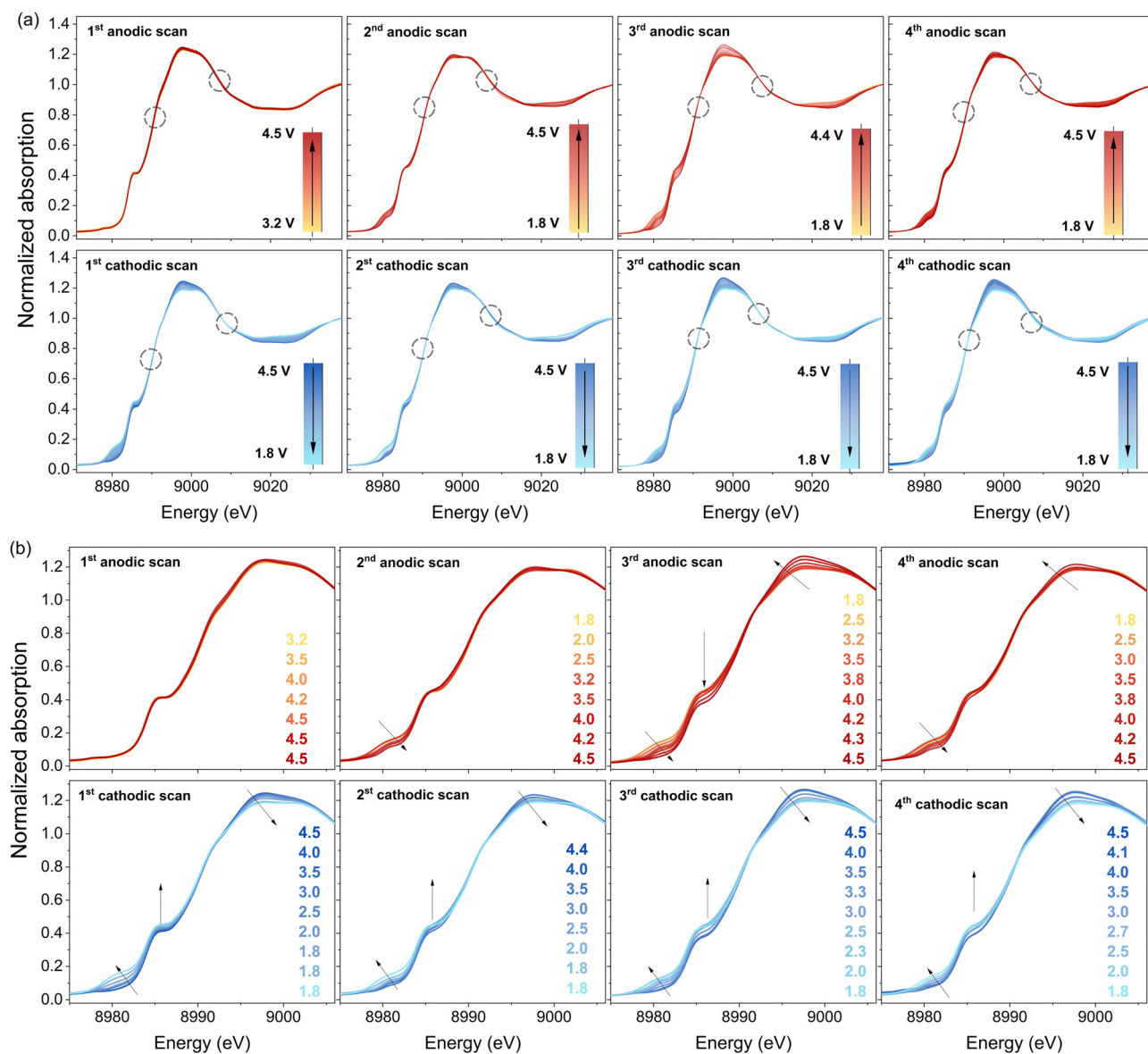

Fig. 4 (a) *Operando* Cu K-edge XANES X of TS-YH-012 cell; (b) highlighted evolution of edge features with spectra from selected voltages. Lighter-colored indicate lower voltages and darker colors for the higher voltages (orange-to-red, light-blue to dark blue). Dashed circles in (a) mark the isosbestic points (indicating two-phase behaviors); arrows in (b) point the direction of spectra evolution.
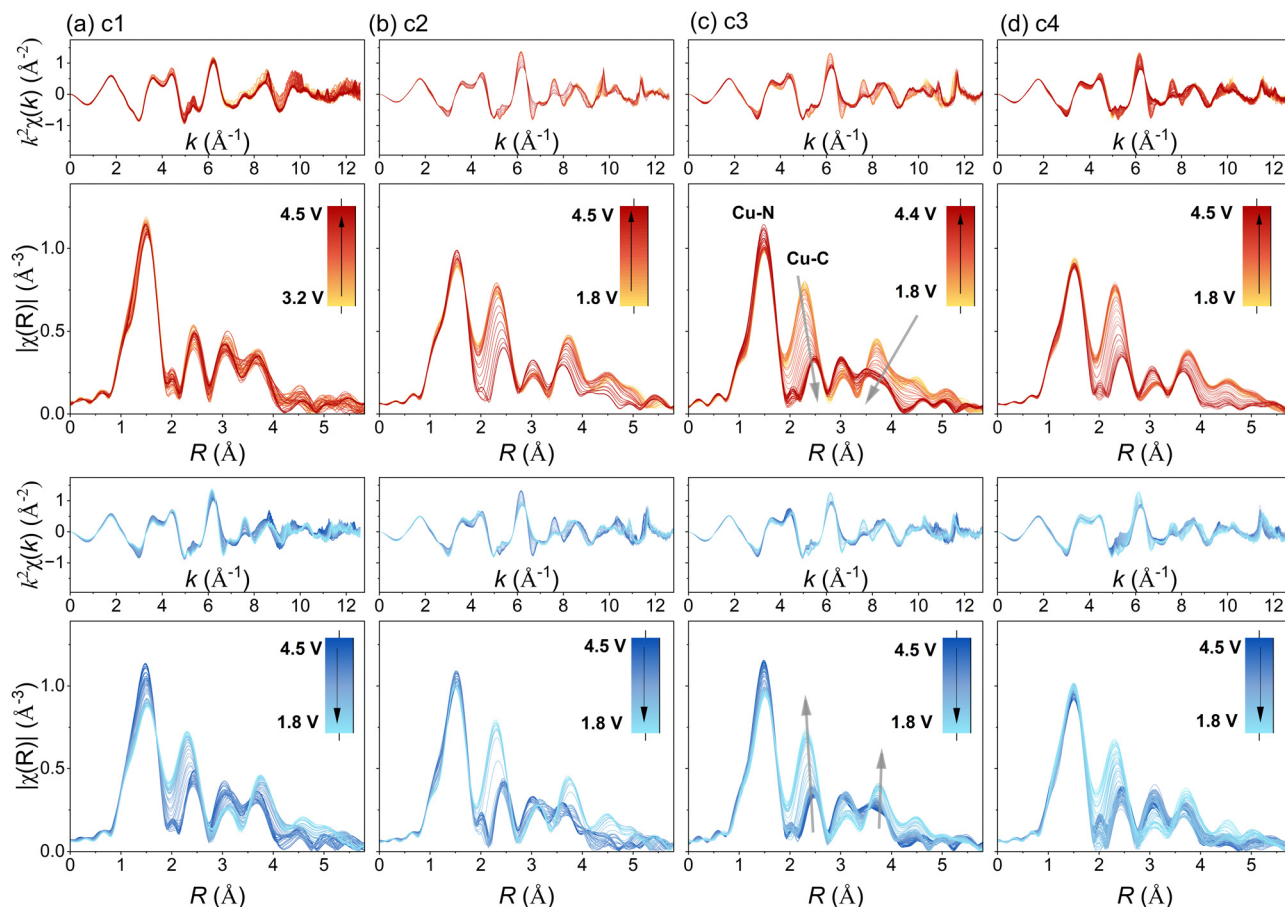
Fig. 5 k^2-weighed $\chi(k)$ spectra of TS-YH-12 cell and the corresponding Fourier transformed magnitude $|\chi(R)|$ during the first four cycles (a–d: c1–c4). The gray arrows in (c) indicates the evolution of amplitudes upon cycling. The phase shift in $|\chi(R)|$ was not corrected so the peak positions are approximately 0.5 Å less than the corresponding interatomic distance.

revert entirely to its original configuration. Secondly, as the observed changes of the oxidation states are subtle, we speculate that a mixture of +I and +II valence states within the overall CuDEPP electrode is present. Some copper centers likely exist in the +I state, while others remain in the +II state. This nuanced interplay could arise from surface-related valence state variations, even as the bulk retains its initial +II state. This conclusion aligns well with prior reports emphasizing the predominantly surface-controlled redox reactions of porphyrins in batteries.[20,23] As calculations show, especially the surface dependence might be related to the insertion degree of lithium into the porphyrin layers making highly loaded structures (three lithium ions intercalated) in the bulk improbable (Fig. S4–S6, ESI†).

Furthermore, CuDEPP demonstrated a gradual change of edge features upon cycling (Fig. S7, ESI†), including the shifts of whiteline and the shoulder on the rising edge, as well as the slight energy shifts at the edge onset. More detailed analyses to clarify the Cu electronic structure are ongoing.

3.4. *Operando* EXAFS

Further corroborating the findings, prominent local structure evolution was evidenced in the EXAFS measurement (Fig. 5). The evolution of $|\chi(R)|$ peaks revealed a progressive modification in

the coordination environment of copper upon cycling. While the Cu–N distance remained relatively stable, the second coordination shell, comprising the next-nearest eight carbon atoms, exhibited substantial changes. Upon charging, the second well-resolved $|\chi(R)|$ peak representing Cu–C shifted to higher R distances with reduced amplitude. This shift implies an increased average interatomic distance, as well as more differentiated Cu–C distances among these eight carbon atoms. Conversely, during discharge, the reverse occurred.

The difference in the average distance between copper and carbon could serve as an indicator of changing aromaticity within the porphyrin. As the carbon atoms alter their electronic structure, their positions (distance Cu–C) may also shift relatively to the copper central atom. Also, the out-of-plane distortion could be explained by carbon atoms coming from neighbouring porphyrin molecules. Notably, the distance between copper and nitrogen remained relatively constant, suggesting that this change is not directly related to a different valence state of copper. Instead, it likely results from a distortion in the π-conjugated system, affecting carbon atom positions and, consequently, the copper-carbon distance. Moreover, the nearly full reversibility of this distance upon recharging strongly correlates with the cycling mechanism. We speculate
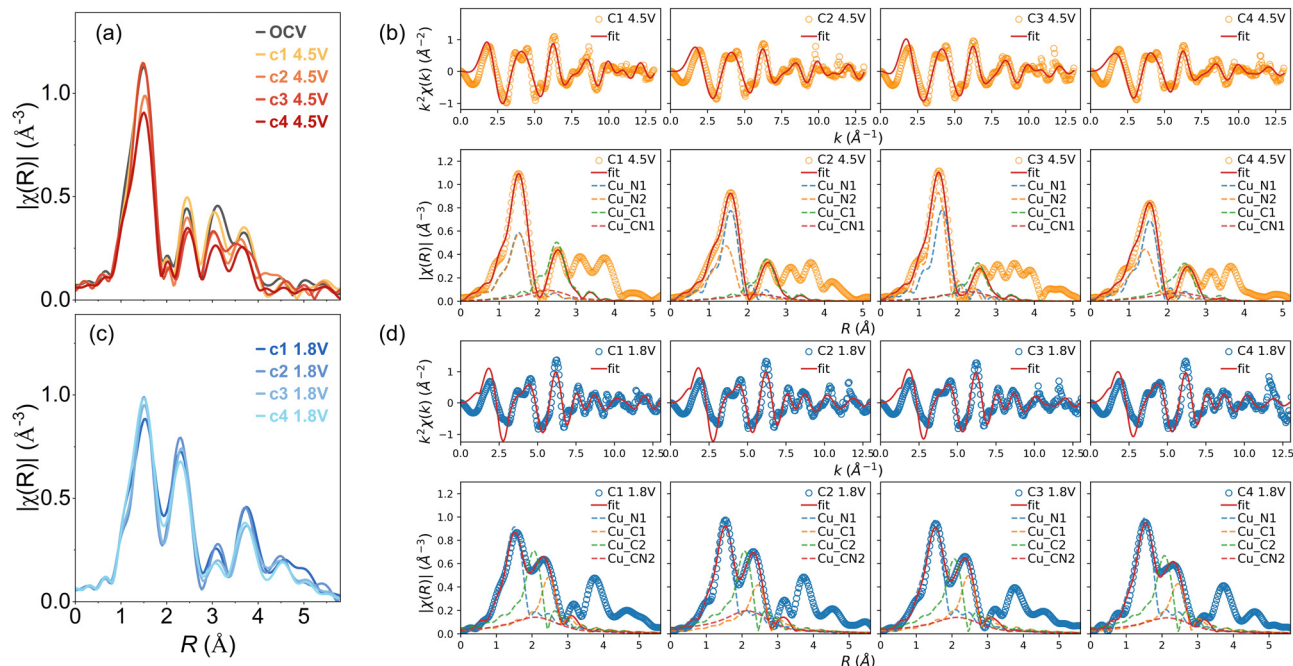
Fig. 6 Comparison in Fourier transformed $|\chi(R)|$ between charged 4.5 V (a) and discharged 1.8 V (c) states; examples of the EXAFS shell fitting: orange and blue circles represent the spectra from charged (b) and discharged (d) states, red lines denotes the fitted results, dash lines indicate the paths included in the fitting. The phase shift was not corrected in $|\chi(R)|$, so the peak positions are approximately 0.5 Å less than the corresponding interatomic distance. The fitted R values and more details on the fitting can be found in the ESI.†

that the obtained data supports the proposed charging mechanism involving an aromaticity switch.[21]

As seen before, also in the EXAFS spectra no major changes could be observed during the first cathodic scan. Neither a prominent change in R direction nor in the amplitude of $|\chi(R)|$ was visible. This behaviour may be attributed to a self-conditioning process, which has been thoroughly studied for CuDEPP materials.[21,23,52]

Moreover, the $|\chi(R)|$ peaks at higher R demonstrated prominent evolution during cycling. According to the FEFF calculation, these features are combinations of all single- and multiple-scattering paths involving both intraplanar and interplanar outer-shell neighbour atoms. A comparative analysis between the highly charged (4.5 V) and discharged (1.8 V) states revealed that the Cu environment change was not entirely reversible (Fig. 6a and c). Especially, the outer-shell peak amplitudes decreased continuously, indicating an increasing disorder during cycling. This trend aligns with the reduced crystallinity observed *via* X-ray diffraction (XRD) and the interplanar separation changes induced by anion intercalations (see ESI†).[21]

The trend propagates with the increased out-of-plane distortion introduced by the insertion of Li$^+$ and PF$_6^-$, as suggested by the theoretical calculation. Therefore, it was impossible to use just one structure model to represent the Cu local environment in EXAFS shell fitting. The only exception constitutes the nearest Cu–N shell, where proper fitting results were obtained. Fig. 6b and d shows the comparison in EXAFS fitting of the CuDEPP at charged (4.5 V) and discharged states (1.8 V), respectively.

For representation of the planar structure of porphyrins the second single-scattering Cu–C path including eight C atoms was

considered. Therefore, a simple model from FEFF calculation of the pristine CuDEPP structure with three paths for the charged states was used. For the discharged states, more structure models were used as significant structural modulations occurred. These structure model suggested 10 carbon atoms for the first Cu–C shell of the second single scattering path. We speculate that this could mean that two carbon atoms are possibly present due to other intermolecular interactions of porphyrins represented in the out of plane disorder. Accordingly, large variations in interatomic distances were observed for these shells (Table S1, ESI†).

Principal component analysis (PCA) hinted at the existence of two distinct intermediates during the cycling of TS-YH-12, consistent with the isosbestic points observed in the XANES region of the absorption spectra. Furthermore, employing multivariate curve resolution with alternating least squares (MCR-ALS), we extracted two pure components—PC1 and PC2—and obtained their concentration profiles (Fig. S8, ESI†).

A qualitative evaluation was conducted by testing the three lithiated structure model on all the spectra (Fig. S9 and S10, ESI†). Except for the first Cu–N coordination shell with relatively stable R and σ_2, the variations for the second Cu–C coordination shell as well as the multi-scattering Cu–C–N paths were significant and cannot be fitted using a single model. In addition, the molecular distortion from the introduction of PF$_6^-$-anion (Fig. S4, ESI†) is worth further investigation.

4. Conclusions

In conclusion, our study represents the first investigation of copper porphyrins using X-ray absorption spectroscopy during

charging and discharging. Through these measurements new evidence was found that during the discharge the copper central atom gets reduced from +II- to +I-oxidation state. However, a mixed material with both oxidation states is observed, where a modest amount of Cu(ɪ) species is present. Importantly, the metal reduction likely occurs primarily at the particle surface. Moreover, the redox process at the copper sites is not fully reversible, as certain environmental changes resist reversion. This intriguing behavior hints at a self-conditioning mechanism, a topic well-discussed in the literature.[21,23,52] Through extensive analysis and fitting of EXAFS results, we also find supporting indications of the aromaticity switch in the charging mechanism. These insights provide a clearer understanding of the processes within porphyrin materials during electrochemical cycling, potentially paving the way for their future development.

Data availability

The experimental and theoretical data generated in this study have been deposited in the Zenodo database under accession code: https://doi.org/10.5281/zenodo.10953950.

Conflicts of interest

The authors declare no conflicts of interest.

Acknowledgements

References

1 J. J. Shea and C. Luo, Organic electrode materials for metal ion batteries, *ACS Appl. Mater. Interfaces*, 2020, **12**(5), 5361–5380.

2 A. Banerjee, N. Khossossi, W. Luo and R. Ahuja, Promise and reality of organic electrodes from materials design and charge storage perspective, *J. Mater. Chem. A*, 2022, **10**(29), 15215–15234, DOI: 10.1039/D2TA00896C.

3 Y. Chen and C. Wang, Designing high performance organic batteries, *Acc. Chem. Res.*, 2020, **53**(11), 2636–2647, DOI: 10.1021/acs.accounts.0c00465.

4 J. Heiska, M. Nisula and M. Karppinen, Organic electrode materials with solid-state battery technology, *J. Mater. Chem. A*, 2019, **7**(32), 18735–18758, DOI: 10.1039/C9TA04328D.

5 G. Milczarek and O. Inganäs, Renewable cathode materials from biopolymer/conjugated polymer interpenetrating networks, *Science*, 2012, **335**(6075), 1468–1471, DOI: 10.1126/science.1215159.

6 A. L. M. Reddy, S. Nagarajan, P. Chumyim, S. R. Gowda, P. Pradhan, S. R. Jadhav, M. Dubey, G. John and P. M. Ajayan, Lithium storage mechanisms in purpurin based organic lithium ion battery electrodes, *Sci. Rep.*, 2012, **2**(1), 960, DOI: 10.1038/srep00960.

7 J.-M. Tarascon, Towards Sustainable and Renewable Systems for Electrochemical Energy Storage, *ChemSusChem*, 2008, **1**(8–9), 777–779, DOI: 10.1002/cssc.200800143.

8 H. Chen, M. Armand, G. Demailly, F. Dolhem, P. Poizot and J.-M. Tarascon, From Biomass to a renewable LiXC6O6 organic electrode for sustainable li-ion batteries, *ChemSusChem*, 2008, **1**(4), 348–355, DOI: 10.1002/cssc.200700161.

9 P. Poizot and F. Dolhem, Clean energy new deal for a sustainable world: from non-CO_2 generating energy sources to greener electrochemical storage devices, *Energy Environ. Sci.*, 2011, **4**(6), 2003–2019, DOI: 10.1039/C0EE00731E.

10 X. Yin, S. Sarkar, S. Shi, Q. A. Huang, H. Zhao, L. Yan, Y. Zhao and J. Zhang, Recent progress in advanced organic electrode materials for sodium-ion batteries: synthesis, mechanisms, challenges and perspectives, *Adv. Funct. Mater.*, 2020, **30**(11), 1908445.

11 Q. Zhao, Y. Lu and J. Chen, Advanced organic electrode materials for rechargeable sodium-ion batteries, *Adv. Energy Mater.*, 2017, **7**(8), 1601792, DOI: 10.1002/aenm.201601792.

12 H. Nishide, Organic redox polymers as electrochemical energy materials, *Green Chem.*, 2022, **24**(12), 4650–4679, DOI: 10.1039/D2GC00981A.

13 C. N. Gannett, L. Melecio-Zambrano, M. J. Theibault, B. M. Peterson, B. P. Fors and H. D. Abruña, Organic electrode materials for fast-rate, high-power battery applications, *Mater. Reports Energy*, 2021, **1**(1), 100008, DOI: 10.1016/j.matre.2021.01.003.

14 C. Ding, C. Li, H. Tian, Y. Tong, W. Huang and Q. Zhang, Recent progress on organic electrode materials for multivalent (Zn, Al, Mg, Ca) secondary batteries, *Batteries Supercaps*, 2022, **5**(7), e202200160.

15 Z. Zhao-Karger, Y. Xiu, Z. Li, A. Reupert, T. Smok and M. Fichtner, Calcium-tin alloys as anodes for rechargeable non-aqueous calcium-ion batteries at room temperature, *Nat. Commun.*, 2022, **13**(1), 3849, DOI: 10.1038/s41467-022-31261-z.

16 Z. Zhao-Karger, P. Gao, T. Ebert, S. Klyatskaya, Z. Chen, M. Ruben and M. Fichtner, New organic electrode materials for ultrafast electrochemical energy storage, *Adv. Mater.*, 2019, **31**(26), 1806599.

17 X. Chen, X. Feng, B. Ren, L. Jiang, H. Shu, X. Yang, Z. Chen, X. Sun, E. Liu and P. Gao, High rate and long lifespan sodium-organic batteries using pseudocapacitive porphyrin complexes-based cathode, *Nano-Micro Lett.*, 2021, **13**(1), 71, DOI: 10.1007/s40820-021-00593-8.

18 F.-Z. Cui, Z. Liu, D.-L. Ma, L. Liu, T. Huang, P. Zhang, D. Tan, F. Wang, G.-F. Jiang and Y. Wu, Polyarylimide and

porphyrin based polymer microspheres for zinc ion hybrid capacitors, *Chem. Eng. J.*, 2021, **405**, 127038, DOI: **10.1016/j.cej.2020.127038**.

19 X. Feng, X. Wu, X. Chen, J. Yuan, S. Lv, B. Ren, X. Sun, E. Liu, S. Tan and P. Gao, A bipolar organic molecule toward a universal pseudocapacitive cathode for stable dual ion charge storage, *Energy Storage Mater.*, 2021, **42**, 454–463, DOI: **10.1016/j.ensm.2021.08.003**.

20 T. Smok, E. Abouzari-Lotf, S. Frentzen, T. Diemant and M. Fichtner, High Active Material Loading in Organic Electrodes Enabled by an in-situ Electropolymerized π-Conjugated Tetrakis (4-Aminophenyl) Porphyrin, *Batteries Supercaps*, 2023, e202300026, DOI: **10.1002/batt.202300026**.

21 P. Gao, Z. Chen, Z. Zhao-Karger, J. E. Mueller, C. Jung, S. Klyatskaya, T. Diemant, O. Fuhr, T. Jacob and R. J. Behm, A porphyrin complex as a self-conditioned electrode material for high-performance energy storage, *Angew. Chem.*, 2017, **129**(35), 10477–10482.

22 S. Lv, J. Yuan, Z. Chen, P. Gao, H. Shu, X. Yang, E. Liu, S. Tan, M. Ruben and Z. Zhao-Karger, *et al.*, Copper porphyrin as a stable cathode for high-performance rechargeable potassium organic batteries, *ChemSusChem*, 2020, **13**(9), 2286–2294, DOI: **10.1002/cssc.202000425**.

23 E. Abouzari-Lotf, R. Azmi, Z. Li, S. Shakouri, Z. Chen, Z. Zhao-Karger, S. Klyatskaya, J. Maibach, M. Ruben and M. Fichtner, A self-conditioned metalloporphyrin as a highly stable cathode for fast rechargeable magnesium batteries, *ChemSusChem*, 2021, **14**(8), 1840–1846.

24 T. Smok, S. Shakouri, E. Abouzari-Lotf, F. Pammer, T. Diemant, S. Jana, A. Roy, Y. Xiu, S. Klyatskaya and M. Ruben, *et al.*, A π-conjugated porphyrin complex as cathode material allows fast and stable energy storage in calcium batteries, *Batteries Supercaps*, 2023, **6**(12), e202300308, DOI: **10.1002/batt.202300308**.

25 X. Chen, X. Feng, B. Ren, L. Jiang, H. Shu, X. Yang, Z. Chen, X. Sun, E. Liu and P. Gao, High rate and long lifespan sodium-organic batteries using pseudocapacitive porphyrin complexes-based cathode, *Nano-Micro Lett.*, 2021, **13**(1), 71, DOI: **10.1007/s40820-021-00593-8**.

26 W. Zhou, M. Yang, Y. Chen, Q. Jing, Q. Fang, Y. Yan and L.-N. Wang, Copper porphyrin within graphene hosts for high-performance lithium-ion battery cathodes, *J. Mater. Sci. Technol.*, 2024, **191**, 192–198, DOI: **10.1016/j.jmst.2023.11.061**.

27 X. Wu, X. Feng, J. Yuan, X. Yang, H. Shu, C. Yang, Z. liu, J. Peng, E. Liu and S. Tan, *et al.*, Thiophene functionalized porphyrin complexes as novel bipolar organic cathodes with high energy density and long cycle life, *Energy Storage Mater.*, 2022, **46**, 252–258, DOI: **10.1016/j.ensm.2022.01.020**.

28 S. Shakouri, E. Abouzari-Lotf, J. Chen, T. Diemant, S. Klyatskaya, F. D. Pammer, A. Mizuno, M. Fichtner and M. Ruben, Molecular engineering of metalloporphyrins for high-performance energy storage: central metal matters, *ChemSusChem*, 2022, e202202090, DOI: **10.1002/cssc.202202090**.

29 F. Neese, Software update: The ORCA program system---Version 5.0, *WIREs Comput. Mol. Biosci.*, 2022, **12**(5), e1606, DOI: **10.1002/wcms.1606**.

30 A. D. Becke, Density-functional thermochemistry. III. The role of exact exchange, *J. Chem. Phys.*, 1993, **98**(7), 5648–5652, DOI: **10.1063/1.464913**, acccessed 3/13/2024.

31 P. J. Stephens, F. J. Devlin, C. F. Chabalowski and M. J. Frisch, Ab Initio Calculation of Vibrational Absorption and Circular Dichroism Spectra Using Density Functional Force Fields, *J. Chem. Phys.*, 1994, **98**(45), 11623–11627, DOI: **10.1021/j100096a001**.

32 S. Grimme, J. Antony, S. Ehrlich and H. Krieg, A consistent and accurate ab initio parametrization of density functional dispersion correction (DFT-D) for the 94 elements H-Pu, *J. Chem. Phys.*, 2010, **132**(15), 154104, DOI: **10.1063/1.3382344**.

33 S. Grimme, S. Ehrlich and L. Goerigk, Effect of the damping function in dispersion corrected density functional theory, *J. Comput. Chem.*, 2011, **32**(7), 1456–1465, DOI: **10.1002/jcc.21759**.

34 F. Weigend and R. Ahlrichs, Balanced basis sets of split valence, triple zeta valence and quadruple zeta valence quality for H to Rn: Design and assessment of accuracy, *Phys. Chem. Chem. Phys.*, 2005, **7**(18), 3297–3305, DOI: **10.1039/B508541A**.

35 J. P. Perdew, K. Burke and M. Ernzerhof, Generalized Gradient Approximation Made Simple, *Phys. Rev. Lett.*, 1996, **77**(18), 3865–3868, DOI: **10.1103/PhysRevLett.77.3865**.

36 H. J. Monkhorst and J. D. Pack, Special points for Brillouin-zone integrations, *Phys. Rev. B: Solid State*, 1976, **13**(12), 5188–5192, DOI: **10.1103/PhysRevB.13.5188**.

37 G. Kresse and J. Furthmüller, Efficient iterative schemes for ab initio total-energy calculations using a plane-wave basis set, *Phys. Rev. B: Condens. Matter Mater. Phys.*, 1996, **54**(16), 11169–11186, DOI: **10.1103/PhysRevB.54.11169**.

38 P. E. Blöchl, Projector augmented-wave method, *Phys. Rev. B: Condens. Matter Mater. Phys.*, 1994, **50**(24), 17953–17979, DOI: **10.1103/PhysRevB.50.17953**.

39 C. La Fontaine, S. Belin, L. Barthe, O. Roudenko and V. Briois, ROCK: a beamline tailored for catalysis and energy-related materials from ms time resolution to μm spatial resolution, *Synchrotron Radiat. News*, 2020, **33**(1), 20–25, DOI: **10.1080/08940886.2020.1701372**.

40 V. Briois, C. La Fontaine, S. Belin, L. Barthe, T. Moreno, V. Pinty, A. Carcy, R. Girardot and E. Fonda, ROCK: the new Quick-EXAFS beamline at SOLEIL, *J. Phys.: Conf. Ser.*, 2016, **712**, 012149, DOI: **10.1088/1742-6596/712/1/012149**.

41 G. Landrot FASTOSH: a software to process XAFS data for geochemical & environmental applications, In Abstracts, Goldschmidt 2018 conference, Boston; 2018.

42 B. Ravel and M. Newville, ATHENA, ARTEMIS, HEPHAESTUS: data analysis for X-ray absorption spectroscopy using IFEFFIT, *J. Synchrotron Radiat.*, 2005, **12**(4), 537–541, DOI: **10.1107/S0909049505012719**.

43 M. Newville, Larch: an analysis package for XAFS and related spectroscopies, *J. Phys.: Conf. Ser.*, 2013, **430**, 012007, DOI: **10.1088/1742-6596/430/1/012007**.

44 M. Newville, P. Livins, Y. Yacoby, J. J. Rehr and E. A. Stern, Near-edge x-ray-absorption fine structure of Pb: A comparison of theory and experiment, *Phys. Rev. B: Condens. Matter Mater. Phys.*, 1993, **47**(21), 14126–14131, DOI: **10.1103/physrevb.47.14126**.

45 M. Newville, EXAFS analysis using FEFF and FEFFIT, *J. Synchrotron Radiat.*, 2001, **8**(2), 96–100, DOI: **10.1107/s0909049500016290**.

46 J.-H. Chou, M. E. Kosal, H. S. Nalwa, N. A. Rakow and K. S. Suslick, Applications of porphyrins and metalloporphyrins to materials chemistry, *Porphyrin Handb.*, 2000, **6**, 43–131.

47 E. B. Fleischer, Structure of porphyrins and metalloporphyrins, *Acc. Chem. Res.*, 1970, **3**(3), 105–112.

48 J. Min Park, J. H. Lee and W.-D. Jang, Applications of porphyrins in emerging energy conversion technologies, *Coord. Chem. Rev.*, 2020, **407**, 213157, DOI: **10.1016/j.ccr.2019.213157**.

49 H.-G. Wang, Q. Wu, L. Cheng, L. Chen, M. Li and G. Zhu, Porphyrin-and phthalocyanine-based systems for rechargeable batteries, *Energy Storage Mater.*, 2022, **52**, 495–513.

50 C. K. Jung, D. Stottmeister and T. Jacob, Properties and Structural Arrangements of the Electrode Material CuDEPP during Energy Storage, *Energy Technol.*, 2020, **8**(9), 2000388, DOI: **10.1002/ente.202000388**.

51 F. Wang, S.-W. Kim, D.-H. Seo, K. Kang, L. Wang, D. Su, J. J. Vajo, J. Wang and J. Graetz, Ternary metal fluorides as high-energy cathodes with low cycling hysteresis, *Nat. Commun.*, 2015, **6**(1), 6668, DOI: **10.1038/ncomms7668**.

52 T. Philipp, G. Neusser, E. Abouzari-Lotf, S. Shakouri, F. D. H. Wilke, M. Fichtner, M. Ruben, M. Mundszinger, J. Biskupek and U. Kaiser, *et al.*, Visualization of structural changes and degradation of porphyrin-based battery electrodes, *J. Power Sources*, 2022, **522**, 231002, DOI: **10.1016/j.jpowsour.2022.231002**.